



Highly doped ZnO films deposited by spray-pyrolysis. Design parameters for optoelectronic applications☆



F.A. Garcés^{a,*}, N. Budini^a, J.A. Schmidt^{a,b}, R.D. Arce^{a,b}

^a Instituto de Física del Litoral (UNL-CONICET), Güemes 3450, Santa Fe S3000GLN, Argentina

^b Facultad de Ingeniería Química, Universidad Nacional del Litoral, Santiago del Estero 2829, Santa Fe S3000AOM, Argentina

ARTICLE INFO

Article history:

Received 29 May 2015

Received in revised form 22 September 2015

Accepted 23 September 2015

Available online 28 September 2015

Keywords:

Spray pyrolysis

Mosaicity

Sol–gel

Zinc oxide

Structural properties

Electrical properties

ABSTRACT

Synthesis and preparation of ZnO films are relevant subjects for obtaining transparent and conducting layers with interesting applications in optoelectronics and photovoltaics. Optimization of parameters such as dopant type and concentration, deposition time and substrate temperature is important for obtaining ZnO layers with optimal properties. In this work we present a study about the induced effects of deposition time on optical and electrical properties of ZnO thin films. These films were deposited by spray pyrolysis of a suitable Zn precursor, obtained through the sol–gel method. The deposition time has direct incidence on internal stress in the crystal structure, generating defects that may affect transparency and electrical transport into the layers. We performed mosaicity measurements, through X-ray diffraction, and used it as a tool to get an insight on structural characteristics and homogeneity of ZnO layers. Also, through this technique, we analyzed thickness and doping effects on crystallinity and carrier transport properties.

© 2015 Elsevier B.V. All rights reserved.

1. Introduction

Transparent conducting oxide (TCO) thin films have been very important concerning the design of devices with immediate applications in sensors, photovoltaics, catalysis, micro- and opto-electronics, among others [1,2]. There are several techniques that allow obtaining TCO thin films, like chemical vapor deposition [3], sputtering [4], electro-deposition [5] and spray pyrolysis [6]. The spray pyrolysis technique possesses important advantages, if compared to others, because it is quite easy to implement and at a relative low cost. It consists basically in subjecting a substrate to a controlled atmosphere where a suitable liquid precursor is sprayed or atomized. If this substrate is maintained at an adequate temperature, a series of chemical reactions is developed, promoting the deposition of a thin film onto it. The stoichiometry of the deposited material is given by the composition of the precursor solution and the chemistry of the reactions that take place. In this way, the chemical composition of the deposited layers can be precisely controlled and the feasibility of simultaneously spraying several precursors gives rise to a broad spectrum of possibilities. The precursors can be obtained *via* the sol–gel method, which allows for an easy control on chemical composition of the final layers. Therefore, the combination of sol–gel and spray

pyrolysis methods provides a tool for designing TCO thin films with optimal properties to be used in diverse fields.

Among the most studied materials for TCO thin films we have chosen intrinsic and doped ZnO, since its physical, electro-optical, piezo-electrical and luminescent properties make it appropriate for a wide range of applications [6–8]. Al-doped ZnO (AZO) in the form of thin films is one of the most studied TCO materials, since it exhibits distinct advantages like abundance in nature, non-toxicity and stability, among others [9].

In previous works we have found that film microstructure strongly influences carrier transport [10,11] by analyzing and correlating variations of structural characteristics induced by thickness or extrinsic dopant effects. Some authors have reported temperature, dopant and thickness effects on the electronic and optical properties of ZnO layers [12,13]. These authors reported structural changes and morphological modifications of the layers caused by thickness increase and dopant effects, but without making emphasis in important issues like crystalline disorder or mosaicity of the films during TCO growth and nucleation processes. Therefore, our proposal is to study the growth process by analyzing the evolution of mosaicity through X-ray diffraction (XRD) measurements of the films as a function of deposition time and dopant concentration. In this work we combined the sol–gel and spray pyrolysis methods to deposit AZO films with different thicknesses, varying deposition time and dopant concentration. In this context, we investigated the effect of film thickening and dopant concentration on the evolution of morphological, electrical and optical properties. The correlation between structural properties, mosaicity and optical and electrical

☆ Revised version submitted to Topical Special Issue on Highly-Doped ZnO and Related Transparent Conductive Oxides.

* Corresponding author.

E-mail address: felipe.garces@santafe-conicet.gov.ar (F.A. Garcés).

properties of the films is discussed. The results presented in this work are particularly interesting for the future development of porous silicon/doped ZnO heterojunctions for optoelectronics applications and sensing devices.

2. Experimental details

For synthesizing the AZO and ethoxylated precursors we used the sol-gel method of Zn salts [Sigma-Aldrich 99.999% $\text{Zn}(\text{O}_2\text{CCH}_3)_2(\text{H}_2\text{O})_2$, 0.2 M] and Al dopant [14]. In this case, the Al source was the $\text{AlCl}_3 \cdot 6\text{H}_2\text{O}$ compound (Sigma-Aldrich 99.0%). The Zn salt was diluted in a mixture of deionized water and ethanol in a 1:9 proportion to get a 0.2 M solution and an equivalent concentration of triethylamine [TEA, Sigma-Aldrich >99% $\text{C}_6\text{H}_{15}\text{N}$] was added to the mixture to act as a chelating agent. Dropwise addition of acetic acid (CH_3COOH) was required to stabilize the pH (at ≈ 7) and avoid precipitation.

We carried out two different experiences, maintaining always a substrate temperature of 450 °C during deposition. First we varied the dopant concentration in the range between 0 and 1.5 at.% by controlling the ratio Al/Zn in the stock solution. It is worth noting that these concentrations correspond to the precursor in solution, while the actual Al concentration in the films might be lower. However, as can be seen in Ref. [15], for Al concentrations below 2 at.% the expected dopant concentration in the film should not differ considerably from that in solution.

As a second experience we fabricated samples with different thicknesses, for which the deposition times were varied in the range from 5 to 30 min (namely 5, 15, 20, 25 and 30 min). These times led to films with thicknesses of 0.43, 0.67, 0.80, 1.26 and 1.44 μm , respectively. Also, we have deposited these TCO films onto porous silicon substrates (see the synthesis and deposition details in [16]) to produce heterojunction devices. TEA was again used as an additive in the sol-gel process. The precursors were gauged in a total volume of 100 mL by using solvents like ethanol and water [17].

We performed XRD measurements in the typical θ - 2θ Bragg-Brentano configuration to have an insight on the structural characteristics of the samples. In this way, we looked for the presence of ZnO characteristic diffraction peaks to ensure that crystalline domains existed in the films. We have normalized XRD patterns to account for thickness differences between samples. Structural mosaicity, or tilting between crystalline domains (as detailed in Ref. [18]), was also determined from XRD measurements. For this, the incidence angle was varied (rocked) in 2° steps around the typical incidence angle of a certain diffraction peak, given by $\theta_{hkl} = 2\theta_{hkl}/2$ for that particular peak, where (hkl) are the Miller indices of the corresponding diffracting plane. For each 2° rocking step of the incidence angle, the diffracted X-ray intensity is scanned in 2θ , as usually, around the maximum of the selected peak, i.e. centered at $(\theta_{hkl}, 2\theta_{hkl})$. This configuration and procedure has been reported by Marty et al. [19] and we have also described it in Ref. [18]. The obtained diffraction patterns were subsequently integrated over the scanned range in 2θ to construct the rocking curves as a function of $\Delta\theta (= \theta - \theta_{hkl})$, whose width measures directly the degree of mosaicity or overall tilting between crystalline domains. The XRD measurements were carried out in a SHIMADZU XD-D1 diffractometer, operating with the Cu $K\alpha$ line ($\lambda = 1.541 \text{ \AA}$).

Film thicknesses were estimated from the interference patterns of the direct transmittance spectra of the samples, measured in a Shimadzu UV3600 spectrophotometer, and were corroborated from measurements performed on scanning electron microscopy images. Surface root-mean-square roughness and texture were inspected by atomic force microscopy (AFM) measurements, in a NANOTEC probe system. In turn, for the electrical characterization we performed measurements of conductivity as a function of temperature under vacuum and Hall effect at room temperature by the Van der Pauw method. The electrical behavior of the heterojunction was determined by measuring

the characteristic current-voltage (J-V) curves using a Keithley 6487 digital picoammeter (see more details of this setup in [16]).

3. Results and discussion

3.1. Doping effect

In Fig. 1 we show the XRD patterns obtained from the deposited AZO samples. For these layers, the characteristic peaks of the hexagonal ZnO structure could be observed. A strong orientation in the $[002]$ direction was evidenced for all Al concentrations, with a texture coefficient (TC) of $\text{TC}(002) = (2.5 \pm 0.3)$ against $\text{TC}(hkl) = (0.25 \pm 0.08)$ for the other crystalline directions. Texture coefficients were calculated as in Ref. [20]. All peaks appeared at the positions corresponding to the wurtzite structure (JCPDS card No. 36-1451) but with differing relative intensities with respect to the powder pattern. We have marked with an asterisk (*) the peak centered at $2\theta \approx 30^\circ$, present in all patterns, which corresponds to the $[044]$ crystalline direction of a secondary zinc oxoacetate phase $[\text{Zn}_4\text{O}(\text{CH}_3\text{COO})_6]$ [21,22]. The inset of Fig. 1 shows a detail of the XRD patterns for $31^\circ < 2\theta < 37^\circ$, where a shifting of the (002) peak to higher angles and an increment of the relative intensity of the peak (101) can be appreciated as the Al concentration increased.

These facts evidence a change in the ZnO structure, since a shifting of the diffraction peaks to higher angles is generally attributed to a diminution of lattice parameters. A shifting of the (002) peak from $2\theta = 34.1^\circ$ to 34.52° was observed as the Al concentration increased. This was attributed to a variation of the lattice parameters in the ZnO crystalline structure, and the analysis was made through the equation

$$\frac{1}{d_{hkl}^2} = \frac{4}{3} \frac{h^2 + hk + k^2}{a^2} + \frac{l^2}{c^2}, \quad (1)$$

where (hkl) describe the crystalline planes, $a = b$ and c stand for the lattice parameters of the hexagonal ZnO structure and d_{hkl} is the characteristic distance between (hkl) planes. In this way, we found that the parameter a decreased from about 3.26 to 3.23 \AA while c diminished from 5.21 to 5.18 \AA , as shown in Table 1. These variations were attributed by Lin et al. to the presence of Al^{+3} ions (with lower radii) that occupy Zn^{+2} sites in the ZnO crystalline structure [23].

In Table 1 we also present the calculated values of crystallite size for each Al concentration in the deposited films. Crystallite size was

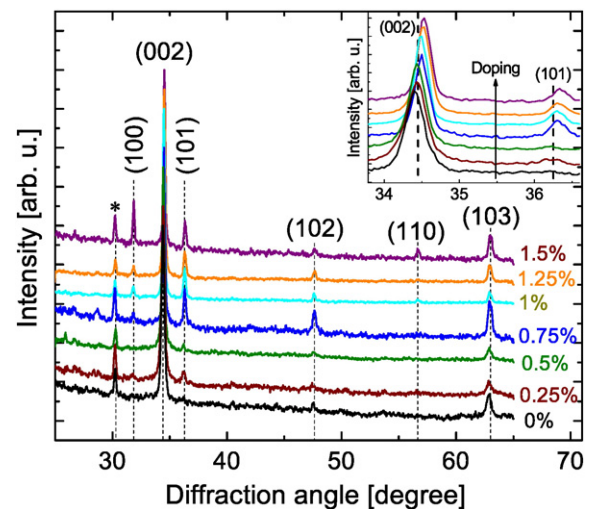


Fig. 1. X-ray diffraction patterns of AZO layers with different Al concentrations in the precursor solution. The characteristic peaks of ZnO can be observed, except for the peak marked with * that corresponds to a different phase. The vertical lines indicate the peak positions of the reference ZnO powder pattern. The inset shows the (002) peak shifting.

Table 1

Calculated values of crystallite sizes and lattice parameters a and c for each Al concentration.

Al concentration (at.%)	Crystal size (Å)	a^* (Å)	c^* (Å)
0.00	328 ± 8	3.258	5.209
0.25	281 ± 13	3.252	5.205
0.50	360 ± 10	3.245	5.202
0.75	437 ± 11	3.244	5.197
1.00	526 ± 7	3.244	5.195
1.25	466 ± 14	3.242	5.192
1.50	538 ± 11	3.236	5.182

* Relative errors below 1%.

calculated from the (0 0 2) peak of the measured XRD patterns (see Fig. 1) through Scherrer's formula [24]. As can be seen, a higher Al concentration resulted in an increase of the crystallite size from 280 to 540 Å. These values are in agreement with those reported by Lin et al. [25].

The structural aspects presented so far are in accordance with the fact that Al acts as an inductor of crystallization, which promotes crystal formation. Therefore, there is an increase of the crystallite size in the layers. The diminution of lattice parameters a and c observed in Table 1 is nearly linear as Al concentration raises. This is in agreement with Vegard's law [26], which allowed corroborating the fact that Al^{+3} ions occupied Zn^{+2} sites in the crystalline structure and caused the observed contraction. The Al^{+3} ions act as donors in ZnO, which enhances the conductivity of the n -type semiconductor. As stated by Shan et al. [27], despite the effectiveness of the Zn^{+2} substitutions by Al^{+3} ions, there might be an accumulation of Al^{+3} ions which tend to form metastable phases and modify the ZnO properties. In our samples we did not detect any phase that could be attributed to Al ions, although there might be amorphous regions of insulating compounds like Al_2O_3 . This compound can be formed in zones of high Al concentration, contributing to the reduction of film conductivity.

We have performed mosaicity measurements to analyze the crystalline structure of the resulting films. For these measurements we chose the (0 0 2) diffraction peak, since it was present in the XRD patterns of all samples. These measurements consist of constructing rocking curves of integrated intensity around the diffraction angle with maximum intensity. The procedure, briefly described in the experimental details section, has been also detailed and optimized in Ref. [18]. The results obtained for these AZO films are shown in Fig. 2. Normally, the contour maps are acquired by varying the angle of incidence θ in 2°

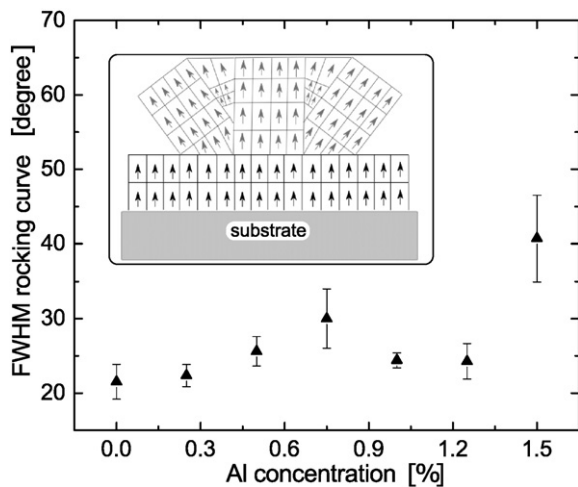


Fig. 2. Full-width at half-maximum values of the rocking curves for the (0 0 2) diffraction peak, as a function of Al concentration in the precursor solution. The inset shows a scheme of crystalline domains misorientation.

steps. For different Al concentrations, the peaks were centered in $\theta = 17.21^\circ$ and $2\theta = 34.4^\circ$. The sample doped with 0.5 at.% of Al presented the most intense peak. In all samples, the peak resulted wider for incident angles well below or above the value at $\theta = 17.21^\circ$. This widening effect indicates that the film loses its initial orientation during growth, which is due to surface roughness and dislocations located at grain boundaries. The mosaicity contour maps for different Al concentrations present a widening of about 8° around the peak centered at $\theta = 17.2^\circ$ ($2\theta = 34.4^\circ$). In some cases this widening was symmetric (for 0.5 at.% and 1 at.% of Al).

The mentioned asymmetries are probably due to internal stress, generated by the presence of a second phase consisting of the zinc oxo-acetate compound, as mentioned before, between successive AZO layers [21]. This secondary phase grows during film deposition and acts as a resetting layer in the ZnO structure (see inset in Fig. 4), which tends to reorient the normal axis of growth (the axis corresponding to the lattice parameter c) as stated by Jiang et al. [28]. The presence of this secondary phase was evidenced by the appearance of the peaks marked with asterisks (*) in the XRD patterns of Fig. 1.

In Fig. 2 we present the full-width at half-maximum (FWHM) evolution of the rocking curves as a function of Al concentration. We see a sharp increase of the FWHM for the two highest dopant concentrations. These values were extracted from fitting Gaussian functions to the rocking curves in order to obtain the misorientation in the layers. There is a relation between surface roughness and mosaicity measurements. The angle between the X-ray source and the detector for the (0 0 2) peak is $180^\circ - 35^\circ = 145^\circ$ and the angle formed by the ZnO crystalline domains oscillates between 120° and 140° [29]. In this way, if the rocking angle increases the signal decreases since the X-rays have to penetrate deeper in the ZnO structure before being diffracted [30].

Fig. 3 shows the residual stress and bond length in the AZO thin films as a function of Al concentration. In-plane stress was calculated using the biaxial strain model [31] and is given by

$$\sigma = \left[2C_{13} - \frac{C_{33}}{C_{13}}(C_{11} + C_{12}) \right] \frac{d-d_0}{d_0}, \quad (2)$$

where C_{ij} are elastic stiffness constants for ZnO ($C_{11} = 207$ GPa, $C_{33} = 209$ GPa, $C_{12} = 118$ GPa, and $C_{13} = 106$ GPa), d is the interplanar spacing for the (0 0 2) peak in our samples and $d_0 = 0.2603$ nm is the corresponding interplanar spacing for a stress-free AZO film. If the stress is positive the biaxial stress is tensile, while if negative the biaxial stress is compressive. The residual stress in our intrinsic ZnO films was smaller than in AZO films, which raised monotonically as the Al concentration increased. This behavior is due to the fact that Al^{+3} ions are occupying Zn^{+2} sites in the crystalline structure, as mentioned above. The total residual stress in the layers consisted mainly in two components: (i) the intrinsic stress, introduced by doping and defects during growth and

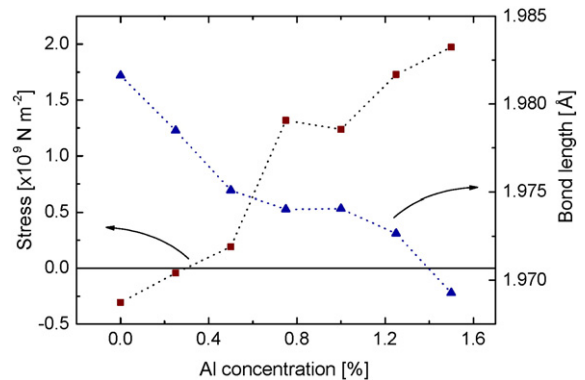


Fig. 3. In-plane stress (left axis) and length of the Zn-O bond (right axis) as a function of the Al concentration in the precursor solution. Negative (positive) values of stress correspond to compressive (tensile) stress.

(ii) the extrinsic stress, produced by the differences in thermal expansion coefficients between the film ($\alpha_{\text{ZnO}} = 2.9 \times 10^6$ 1/K) and the substrate ($\alpha_{\text{glass}} = 7.2 \times 10^6$ 1/K). This latter component contributes slightly to stress in the films at room temperature since deposition was made at 450 °C. In our films, deposition temperatures were kept the same. Therefore, the stress originating from thermal mismatch between sample and substrate was expected to be of the same magnitude for all samples. In this way, the observed change in the residual stress of the AZO films was attributed mainly to Al doping and corresponding changes in the ZnO structure, resulting from the change in Zn–O bond length (L) described as

$$L = \sqrt{\frac{a^2}{3} \left(\frac{1}{2} - u \right)^2} c^2, \quad (3)$$

where u in the wurtzite structure is related to the a/c ratio as

$$u = \frac{a^2}{3c^2} + 0.25. \quad (4)$$

In our films, the bond length decreased as the Al concentration augmented. This trend is inverse in comparison with that of residual stress. So, the observed behavior is attributed to the contraction of the interplanar distance by the $\text{Al}^{+3} - \text{Zn}^{+2}$ substitution, which causes a shrinkage of the crystalline structure along the c axis.

Hall effect measurements evidenced a n -type character of the AZO films. The resistivity (ρ), carrier density (n) and mobility (μ) values as a function of Al concentration are shown in Fig. 4(a) and (b). As seen in Fig. 4(a), the resistivity of the material decreased about one order of magnitude as the Al concentration increased from 0 at.% to 1 at.%, presenting an abrupt increment for higher concentrations. In turn, n and μ reached a maximum for an Al concentration of 1 at.% with values of

$5.5 \times 10^{19} \text{ cm}^{-3}$ and $50 \text{ cm}^2/(\text{V s})$, respectively. For Al concentrations above 1 at.% both parameters diminished. The obtained mobilities in this work are quite similar to those reported by Sagar et al., of about $53 \text{ cm}^2/(\text{V s})$, for AZO samples deposited through the spin-coating technique from sol–gel derived precursors [32]. Shinde et al. have obtained lower resistivity and higher mobility values for almost the same values of carrier densities ($n \sim 10^{19} \text{ cm}^{-3}$) in fluorine-doped ZnO films deposited by spray-pyrolysis at doping levels between 5 and 20 at.% [20]. By using concentrations from 1 and 4 at.% of indium as dopant ($n \sim 10^{20} \text{ cm}^{-3}$), Shinde et al. also obtained more conductive films but with lower mobilities in comparison with our samples [33].

The variations observed for n and μ can be understood in terms of the position of Al ions inside the ZnO structure. Generally, ZnO grows as a n -type semiconductor, due to the presence of native defects such as interstitial atoms or oxygen vacancies. The behavior observed in our samples, for Al concentrations below 1 at.%, can be explained through the substitutional nature of Al^{+3} doping ions in the ZnO structure. This is in accordance with the observed variations of lattice parameters and residual stress in the films, shown above. As a result of this process, an extra contribution of free electrons into the conduction band appears. Besides this, the diminution of n and μ for Al concentrations above 1 at.% can be attributed to the alternative interstitial mode of Al^{+3} ion incorporation into the ZnO structure. This process tends to generate distortions in the crystalline structure. Moreover, the presence of these ions in interstitial sites and grain boundaries produces scattering, which is detrimental for mobility. In turn free carrier density diminution can be attributed to segregation of Zn to the secondary zinc oxoacetate phase, reducing doping efficiency. This is also evidenced by the increase of structural disorder (*i.e.* FWHM of rocking curves, Fig. 2) for higher Al concentrations. We remark here that the film with better electrical properties (with about 1 at.% of Al) also possessed a small FWHM value, indicating a lower disorder.

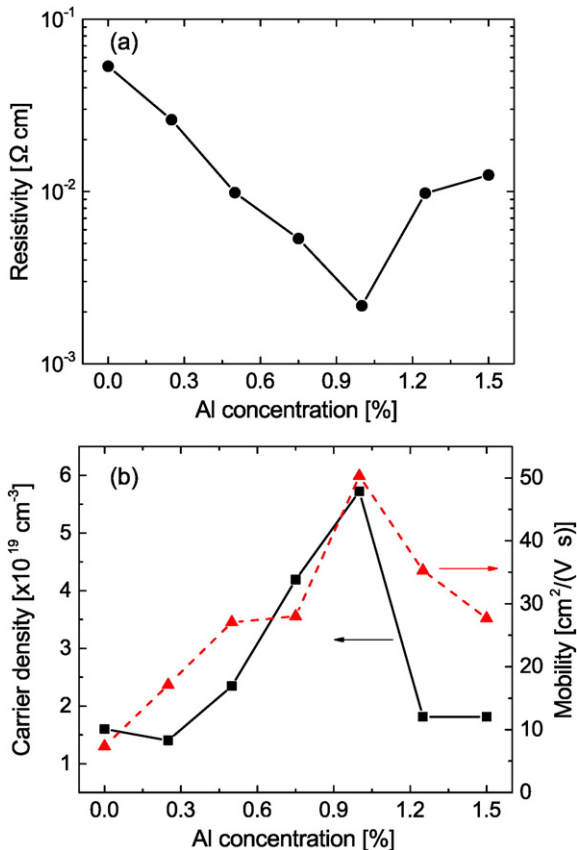


Fig. 4. Evolution of (a) resistivity and (b) carrier concentration and Hall mobility as a function of Al concentration in the precursor solution.

3.2. Thickness effect

We deposited a series of samples with different thicknesses (just varying the deposition time) to investigate how thickening affects structural and electrical properties of AZO films. As is deduced from the thickness value obtained for each deposition time (see Experimental Details), we could determine that the only sample with significantly different growth rate was that deposited during 5 min ($\approx 86 \text{ nm/min}$). The mean growth rate for the rest of the samples (deposited during 15, 20, 25 and 30 min) was about $(46 \pm 4) \text{ nm/min}$. A higher growth rate during the first stages of deposition can be reasonably attributed to the intrinsic dynamics of the process. Growth onto the glass substrate (right at the beginning) should differ from growth onto the ZnO film itself (for longer times). Besides this, as the film thickens several phenomena appear, such as nucleation, stress and relaxation, which should also produce variations in growth rate to some extent. This explanation is consistent with the fact that for longer deposition times the growth rate was quite stable.

In Fig. 5 we show the XRD patterns of AZO films, in which all samples presented the characteristic diffraction peaks of the hexagonal wurtzite ZnO structure. In this case, the doping concentration was fixed at 1 at.% and the secondary zinc oxo-acetate phase (see Fig. 1) was not observed. However, we did find a spinel secondary phase of ZnAl_2O_4 , whose peak was centered at $2\theta = 38.55^\circ$ and was present in all samples [34]. The thinnest sample presented three clear diffraction peaks, namely (1 0 1), (0 0 2) and (1 0 3), evidencing a strong orientation in the [0 0 2] direction.

The preferential orientation of the ZnO c axis in the films leads to an enhancement of the (0 0 2) diffraction peak [35,36]. In our films, for thicknesses greater than $0.80 \mu\text{m}$, the (1 0 1) and (1 0 3) peaks appeared more defined while the (0 0 2) peak remained as dominant. In turn, when the thickness increased to around $1.44 \mu\text{m}$ ($\approx 30 \text{ min}$) the (0 0 2) diffraction peak was still dominant, with $\text{TC}(002) = (2.6 \pm 0.1)$, and the others

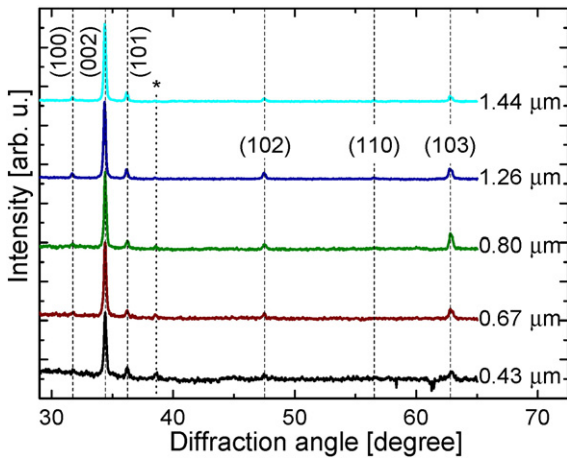


Fig. 5. X-ray diffraction patterns of AZO layers with different thicknesses. A preferential (0 0 2) orientation can be observed. The peak marked with * corresponds to a secondary phase different from ZnO.

peaks resulted slightly diminished, yielding $TC(hkl) = (0.19 \pm 0.08)$ in average. As before, TC values were calculated as in Ref. [20]. Some authors have suggested that for thick enough AZO films, the surface tends to be oriented in the [0 0 2] direction due to its lower surface energy [37]. The fact that such small intensities were observed for the (1 0 1), (1 0 2) and (1 0 3) diffraction peaks can be attributed to a growth competition between neighboring growing crystalline domains according to their orientations. The faster growing crystals will grow over slower ones. This competitive growth represents an orientation selection among the crystals and results in what is called the competitive growth texture [38], which explains the diminished intensity of these diffraction peaks in our samples [24]. To further investigate the difference between the films exhibiting a *c*-axis, or (0 0 2) preferential orientation, and the intensity reduction of the other diffraction peaks, we again performed mosaicity measurements by XRD. As before, this allowed us to analyze the crystalline homogeneity of films with different thicknesses. The rocking curves around the diffraction angle of maximum intensity for the (0 0 2) peak were obtained as described before.

In Fig. 6 we show the FWHM evolution of the rocking curves for the (0 0 2) peak as a function of roughness. We remark here that roughness increased almost linearly with film thickness. A typical rocking curve is shown in the inset of Fig. 6 for the 0.43 μm sample, that corresponds to lowest roughness. The FWHM increased from 12.8° for a roughness value of 25 nm to 18° for 46 nm. For the highest roughness (67 nm)

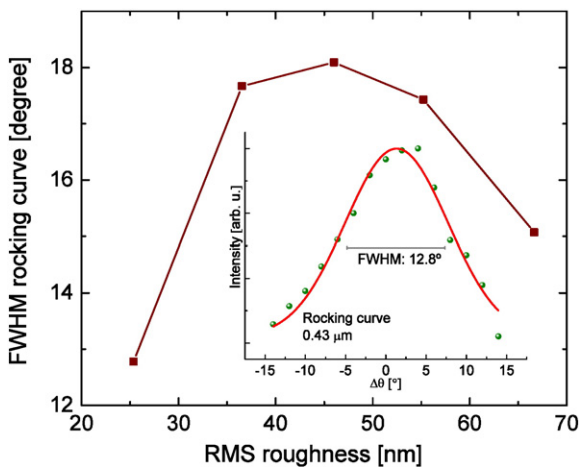


Fig. 6. Full-width at half-maximum values of the rocking curves for the (0 0 2) diffraction peak, as a function of roughness of the films. The inset shows the fitting procedure for the sample deposited during 5 min.

the FWHM decreased to 15°. These FWHM values revealed the average uniformity of the *c* axis and, consequently, better crystalline quality. The variation of FWHM with roughness is also due to stress in the films. In an epitaxial growth, it is generally expected that thicker films exhibit smaller FWHM values and higher crystalline quality. This can be explained as follows. During the first stages of deposition there is an important structural mismatch between growing film and substrate, producing a large strain within the growing film and disturbing the uniformity of the *c* axis orientation. As the film grows, the strain between newer and older layers is relaxed and a more ordered structure results. This yields a rocking curve with a reduced FWHM [30,39,40].

The FWHM values of our samples presented a different behavior as a function of roughness, which we attributed to the fact that films may not grow epitaxially onto the glass substrates. During initial growth stages, as said before, various grain orientations compete [41]. Also, the average grain size increases as the fastest growing grains dominate over differently oriented neighboring grains. In this case, the nucleation density is greater than the grain density. In our case, consequently, a maximum value of the FWHM was observed for the film with a roughness of 46 nm. This was attributed to the presence of internal strain. For thicker films the strain is relaxed, as mentioned above, leading to a subsequent FWHM diminution. Therefore, the FWHM curve of Fig. 6 clearly shows a transition point from high to low stress for a roughness value of 46 nm.

Using Eq. (2) (biaxial strain model) we calculated in-plane stress. The resulting values are plotted in Fig. 7. The negative sign of σ indicates that the stress in the films is compressive. It may be noted that in this case, we only modified the thickness of the layer. Therefore, the thermal expansion coefficients between AZO films and substrate were the same in all of them. Moreover, in general, the internal stress varies during film growth as explained in the following paragraph. Generally, in polycrystalline thin films, there are different regimes of internal stress during film growth. First, during the early nucleation stage (*i.e.* before the film has coalesced) compressive stress is attributed to the effect of surface capillary forces on isolated clusters [42]. Subsequently, when these clusters coalesce to form a fully continuous film, this compressive stress increases (*i.e.* residual stress becomes more negative). This is attributed to an increase in the surface chemical potential that is known to induce atoms to flow into grain boundaries, which also increases compressive stress in the film [43]. In this context, as is observed in Fig. 7, all of our films had compressive stress. For thicker films, compression resulted greater due to atoms flowing to grain boundaries [42–44].

In our case, the residual (compressive) stress as a function of roughness presented a transition point at 46 nm. From this point we could see a different behavior, after which the values of compression diminished to $-1.35 \times 10^9 \text{ N/m}^2$ for a roughness of 55 nm. Hence, as thickness

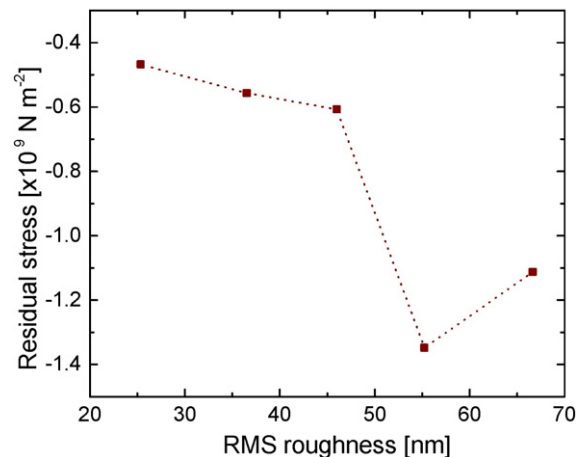


Fig. 7. In-plane stress as a function of roughness for the series of AZO samples. The negative values indicate a compressive stress.

increased the film reached a point at which the crystalline misorientation is maximum and stress relaxation occurs (at this point the FWHM decreased slightly). That effect allows the growth to reset and, therefore, successive layers start to growth ordered.

In Fig. 8 we show the variation of carrier concentration and Hall mobility as a function of roughness. We could see a linear increase of carrier concentration as samples thickened, which was of about three orders of magnitude. On the other hand, there was a decrease of carrier mobility. Normally, these parameters are affected by doping variations. In our case, the dopant concentration was kept constant in the precursor solution. Sometimes, this concentration yields different doping levels in the deposited films. Furthermore, the carriers may in part be excited from native defects such as interstitial Zn atoms and/or oxygen vacancies [45]. Therefore, the carrier concentration shown in Fig. 8 accounts for all free electrons excited from Al atoms and native defects. In consequence, we conclude that Al atoms and native defects, both acting as donors, increased free carrier concentration as the films thickened. On the other hand, the ZnO films showed low conductivity due to the chemisorption of oxygen [46,47] at grain boundaries (we recall that air was used as gas carrier during deposition). When the deposition is performed at low temperatures ($\approx 150^\circ\text{C}$) [46], oxygen is chemisorbed in the film both at grain boundaries and at the surface. Those grain boundaries appeared due to the misorientation as the films thickened. An evidence of this can be observed in Fig. 8, where the carrier concentration increased continuously as the films thickened. The rapid cooling at the end of deposition does not allow oxygen to escape from the sample. However, considering the higher temperature used in this work (450°C), oxygen would have more available thermal energy to escape and increase the final carrier concentration of the samples. So, adsorbed oxygen may produce potential barriers which hinder the electrical transport. The principal chemisorption species in ZnO are O_2^- at low temperatures. When deposition temperature raises, the chemisorbed O_2^- desorbs from the sample and donates an electron to ZnO (*i.e.* $\text{O}_2^- \rightarrow \text{O}_2 + e^-$) [47]. This reaction produces an increase of film conductivity. Besides this, we can consider that the surface area of the sample increased as it thickened, which also increased the fraction of free electrons trapped by chemisorbed oxygen that were subsequently donated during oxygen desorption. This fact was evidenced by the results showed in a previous work [10], where the shift in the absorption edge was attributed to a higher carrier concentration [48,49].

As is also observed in Fig. 8, Hall mobility decreased for thicker samples. Carrier mobility is related to macroscopic and microscopic imperfections in the films. At the macroscopic level we include grain boundaries, internal stress and surface roughness, all of which can be observed in our samples. In turn, the microscopic level accounts for ionized donors and neutral impurity atoms. In ZnO, particularly, a surface barrier is created by the chemisorption of oxygen, which considerably

reduces carrier mobility. Besides this, grain boundaries are also considered to be effective inhibitors of carrier mobility [46].

Carrier mobility in thinner AZO films, with lower roughness, resulted strongly dependent on thickness. We consider that the thickness dependence of mobility in AZO films is mainly due to a variation in the density of scattering centers, such as lattice strain points, and dislocations caused by misorientation between crystalline domains (mosaicity). The mobility of the film with the highest roughness (67 nm) reached a minimum value, although the FWHM value of its rocking curve was slightly lower than for the sample with a roughness value of 55 nm. This might be indicating that the defect density increased for higher deposition times and that other scattering centers (such as grain boundaries) were introduced in the film. Thus, we conclude that the density of scattering centers increased with deposition time, resulting in reduced carrier mobility.

The electrical conductivity can be modeled as an activated process, following the Arrhenius law in a wide temperature range [50]. In ZnO, the activation energy is related to localized states in the semiconductor gap and is generally taken as the energy difference between the minimum (maximum) of the conduction (valence) band and the Fermi energy, if the semiconductor is *n*-type (*p*-type).

Fig. 9 shows the activation energies (E_a) calculated by fitting of the Arrhenius plots of current as a function of temperature. The obtained values were all in the range between 20 and 60 meV, which is in good agreement with other works [51]. As mentioned before, we attribute these very low activation energies to grain boundary effects dominating carrier mobility. The presence of grain boundaries was evidenced by the existence of a high degree of mosaicity between crystalline domains in the samples and marked by a transition point for the sample with a roughness value of 46 nm. The defective structure of grain boundaries is known to contribute with localized defect states in the material band gap which may act as traps or recombination centers. In thicker films, with a higher degree of mosaicity, these effects become more important and are mainly mediated by oxygen ions chemisorbed in ZnO boundaries, as discussed above. Therefore, when these species are desorbed they donate an electron to ZnO (see reaction above [47]). As these electrons are trapped they set up a negative charge at the grain boundaries, generating a spatial charge region extending into the grains and giving place to the observed low activation energies. This is consistent with the observed diminution of the activation energy for thicker samples, which is due to the presence of a higher amount of intrinsic defects in the films, and is also consistent with the lower mobility of the sample with the highest roughness (67 nm), because of higher carrier density. It is worth noting here that the E_a value of the sample with lowest carrier density should have been higher, following the expected linear diminution of E_a as a function of carrier density in the presented semilog plot. However, for the lowest carrier density

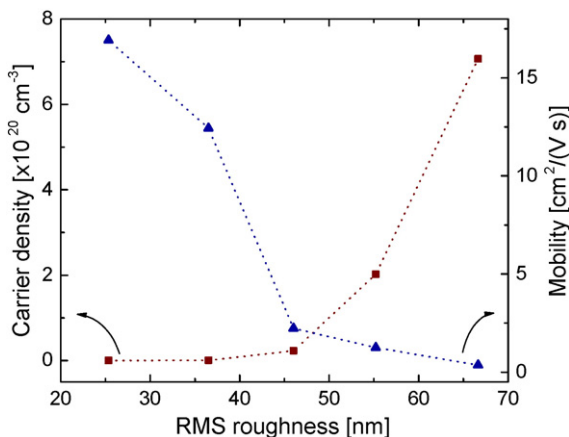


Fig. 8. Carrier density (left axis) and Hall mobility (right axis) as a function of roughness for the series of AZO samples. Lines are only a guide to the eye.

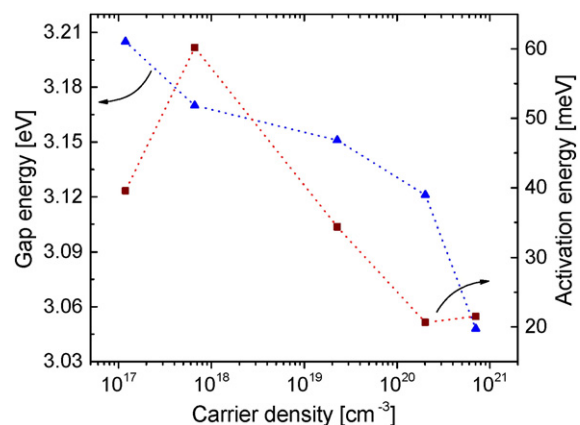


Fig. 9. Gap energy (left axis) and activation energy of dark conductivity (right axis) as a function of carrier density for the series of AZO samples with different thicknesses.

($\approx 1 \times 10^{17} \text{ cm}^{-3}$) E_g resulted lower than expected. This might be due to non-effective doping at low doping levels.

On the other hand, in Fig. 9, we show the gap values obtained by extrapolation of the linear region on the absorption coefficient. These values decreased linearly as carrier concentration increased. It is well-known that two competing phenomena affect the band gap energy values as donor density increases, mainly in heavily doped semiconductors [35]. The first is related to a gap widening and is known as Burstein-Moss effect [48]. The second phenomenon affects the gap of ZnO for carrier concentrations above the Mott critical concentration ($\approx 5 \times 10^{18} \text{ cm}^{-3}$) because electron–electron and electron–impurity interactions give rise to an energy shift of the valence and conduction bands, reducing the band gap [35]. This has been attributed to the merging of an impurity band into the conduction band, thereby shrinking the band gap.

Our results indicate that the shrinkage effect is the dominant phenomenon, which is evidenced by the diminution of optical gap values as carrier concentration increases.

Besides the fact that grain boundaries dominate because of their much higher density of defects, there is also a small contribution from defects inside crystalline domains, like Zn interstitials (Zn_i) and oxygen vacancies (V_o). Also the group-III impurities like Al act as shallow donors in ZnO when substituting Zn atoms. The extra valence electron of these impurities is loosely bound and occupies effective-mass states near the conduction band minimum at low temperatures. As the temperature rises, this extra electron is easily excited to the conduction band.

3.3. ZnO:Al heterojunctions

Normally, TCO films are used as frontal protection and electrical contact in solar cells. In this work, we used an improved AZO film (designed as a function of the studied parameters mentioned in the previous sections). Fig. 10(a) shows a scanning-electron microscopy image of a macro-porous silicon (MPS) substrate, obtained by electrochemical process. The porous silicon methodology was reported in previous works [16,52]. Also, we observe an AZO layer deposited by the spray pyrolysis technique during 20 min, seen as hexagonal structures in the inset of Fig. 10(a). The spray pyrolysis process, leading to the formation of AZO grains on the external surface and inside the pores, generates grains sizes of around 80 nm. These particles were present at the surface and within the porous structure.

Fig. 10(b) shows the J–V characteristic curve of the MPS/ZnO:Al heterojunction in the range between -3 V to $+3 \text{ V}$ and in a semilog plot. The voltage was applied between a golden pin front contact and aluminum back contact, as shown in the inset of Fig. 10(b). Devices with this configuration are usually rectifying due to the formation of interface barriers. The associated carrier transport mechanisms are similar to those observed in a normal p – n heterojunction [53], showing a rectification ratio in darkness of approximately 400 at $\pm 3 \text{ V}$. The rectification ratio for this J–V curve obtained in dark was approximately 100 at $\pm 3 \text{ V}$. In the reverse bias region, an increase in the photogenerated current could be observed when illumination was applied. The current was only modified in the reverse bias and increased by more than two orders of magnitude with respect to the current in the dark condition. The values of open-circuit voltage and short-circuit current were about 132 mV and 3.2 mA/cm^2 , respectively, under an illumination of 110 mW/cm^2 .

The experimental data presented in Fig. 10(b) were fitted with a simple diode model [53]. As a result, we obtained the following set of parameters: series resistance (R_s), parallel resistance (R_p), reverse saturation current (I_0) and ideality factor (n). Although these J–V curves perfectly fit with the simple diode model in dark and under illumination, subtle changes in the fitting parameters occur when moving from one situation to another. Values in dark conditions are $n = 2$, $I_0 = 0.16 \text{ mA/cm}^2$, $R_s = 31 \Omega$ and $R_p = 2.7 \times 10^4 \Omega$. On

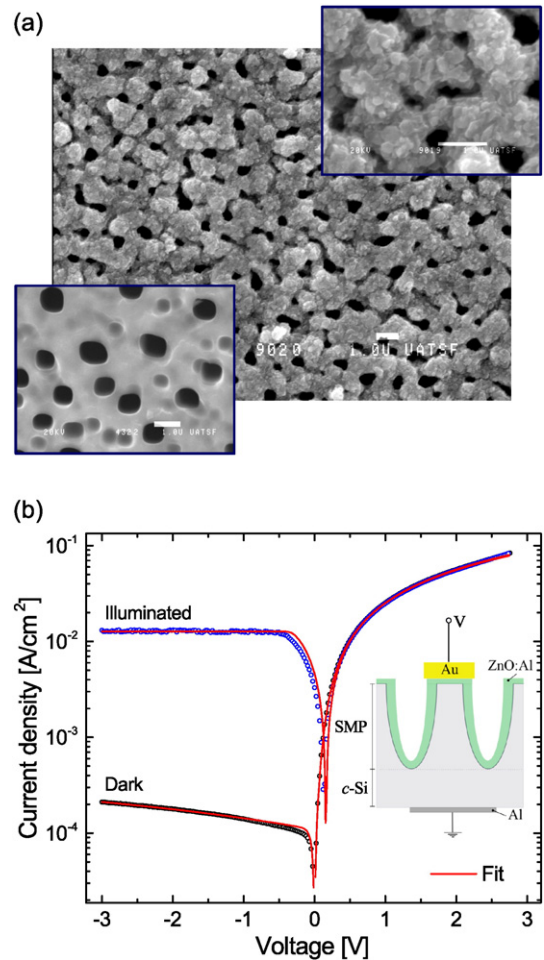


Fig. 10. (a) Scanning electron microscopy images of AZO films deposited onto macroporous silicon (the top inset is a sample with AZO and the bottom inset is a sample without AZO); (b) current–voltage characteristics of macroporous silicon/AZO heterojunctions, at dark and illuminated conditions. A fit with a simple diode model is included for each case.

the other hand, the parameters for the illumination situation are $n = 7$, $I_0 = 12 \text{ mA/cm}^2$, $R_s = 30 \Omega$ and $R_p = 2.3 \times 10^4 \Omega$.

4. Conclusion

We have obtained AZO thin films onto glass with different thicknesses through spray pyrolysis deposition of sol–gel synthesized precursors at a temperature of $450 \text{ }^\circ\text{C}$. We analyzed the correlation between morphological characteristics (roughness, grain size, preferential orientation, mosaicity) with electrical characteristics (conductivity, mobility, carrier concentration) and their variations with film thickness. For an Al concentration of 1.0 at.% we obtained a relatively high conductivity of about $500 \Omega^{-1} \text{ cm}^{-1}$ and the highest Hall mobility of about $50 \text{ cm}^2 \text{ V}^{-1} \text{ s}^{-1}$. Mosaicity was seen to increase with film thickness. We also studied the effect of Al concentration on structural properties, concluding that a higher doping level affected mainly the a and c lattice parameters. We analyzed the effects of stress and mosaicity on structural and electrical properties of the films, which provided us important information about the growth mechanism associated to the spray pyrolysis method. The results presented demonstrate a strong correlation between growth parameters and electrical properties of ZnO films. In particular, thickening has a marked effect on carrier concentration and activation energies for electrical conduction, attributed mainly to the defective structure of grain boundaries. Hence, tuning precursor obtention and spray pyrolysis deposition parameters it is possible to

improve the design of photovoltaic and optoelectronic devices based on AZO films. Specifically, we presented the first steps towards the development of porous silicon/doped ZnO heterojunctions.

Acknowledgments

This work was supported by projects from ANPCyT (PICT 32515), Universidad Nacional del Litoral (CAID 2009/68–343) and CONICET (PID 0414) institutions from Argentina.

References

- P.D.C. King, T.D. Veal, Conductivity in transparent oxide semiconductors, *J. Phys. Condens. Matter* 23 (33) (2011) 334214.
- S. Shinde, K. Rajpure, High-performance UV detector based on Ga-doped zinc oxide thin films, *Appl. Surf. Sci.* 257 (22) (2011) 9595–9599.
- A. Abrutis, L. Silimavicius, V. Kubilius, T. Murauskas, Z. Saltyte, V. Plausinaitiene, Doped zinc oxide films grown by hot-wire chemical vapour deposition, *Thin Solid Films* 576 (2015) 88–97.
- N. Sommer, S. Götzendörfer, F. Köhler, M. Ziegner, J. Hüpkes, Influence of deposition conditions and substrate morphology on the electrical properties of sputtered ZnO:Al grown on texture-etched glass, *Thin Solid Films* 568 (2014) 25–30.
- J. Chen, J. Chen, D. Chen, Y. Zhou, W. Li, Y. Ren, L. Hu, Electrochemical deposition of Al-doped ZnO transparent conducting nanowire arrays for thin-film solar cell electrodes, *Mater. Lett.* 117 (2014) 162–164.
- M.A. Mahadiq, Y.M. Hunge, S.S. Shinde, K.Y. Rajpure, C.H. Bhosale, Semiconducting properties of aluminum-doped ZnO thin films grown by spray pyrolysis technique, *J. Semicond.* 36 (3) (2015) 033002.
- M. Hussain, A. Khan, O. Nur, M. Willander, E. Broitman, The effect of oxygen-plasma treatment on the mechanical and piezoelectrical properties of ZnO nanorods, *Chem. Phys. Lett.* 608 (2014) 235–238.
- E.M. Likovich, R. Jaramillo, K.J. Russell, S. Ramanathan, V. Narayanamurti, Narrow band defect luminescence from Al-doped ZnO probed by scanning tunneling cathodoluminescence, *Appl. Phys. Lett.* 99 (15) (2011) 151910.
- K. Ravichandran, N.J. Begum, S. Snega, B. Sakthivel, Properties of sprayed aluminum-doped zinc oxide films—A review, *Mater. Manuf. Process.* (2014) 1–13.
- F.A. Garcés, N. Budini, R.D. Arce, J.A. Schmidt, Effect of thickness on structural and electrical properties of Al-doped ZnO films, *Thin Solid Films* 574 (2015) 162–168.
- F.A. Garcés, N. Budini, J.A. Schmidt, R.D. Arce, Structural analysis of ZnO:(Al,Mg) thin films by X-ray diffraction, *Proc. Math. Sci.* 8 (2015) 551–560.
- D. Miao, S. Jiang, S. Shang, Z. Chen, Effect of heat treatment on infrared reflection property of Al-doped ZnO films, *Sol. Energy Mater. Sol. Cells* 127 (2014) 163–168.
- G. Kenanakis, N. Katsarakis, E. Koudoumas, Influence of precursor type, deposition time and doping concentration on the morphological, electrical and optical properties of ZnO and ZnO:Al thin films grown by ultrasonic spray pyrolysis, *Thin Solid Films* 555 (2014) 62–67.
- L. Znaidi, Solgel-deposited ZnO thin films: A review, *Mater. Sci. Eng. B* 174 (13) (2010) 18–30.
- F. Paraguay D, J. Morales, W.E. Estrada L, E. Andrade, M. Miki-Yoshida, Influence of Al, In, Cu, Fe and Sn dopants in the microstructure of zinc oxide thin films obtained by spray pyrolysis, *Thin Solid Films* 366 (12) (2000) 16–27.
- F.A. Garcés, R. Urteaga, L. Acquaroli, R.R. Koropecski, R.D. Arce, Current–voltage characteristics in macroporous Si/SiO₂/SnO₂:F heterojunctions, *Nanoscale Res. Lett.* 7 (1) (2012) 419.
- R.R. Biswal, S. Velumani, B.J. Babu, A. Maldonado, S. Tirado-Guerra, L. Castaeda, M. de la L. Olvera, Fluorine doped zinc oxide thin films deposited by chemical spray, starting from zinc pentanedionate and hydrofluoric acid: effect of the aging time of the solution, *Mater. Sci. Eng. B* 174 (13) (2010) 46–49.
- F.A. Garcés, N. Budini, R.R. Koropecski, R.D. Arce, Structural mosaicity and electrical properties of pyrolytic SnO₂:F thin films, *Thin Solid Films* 531 (2013) 172–178.
- B. Marty, P. Moretto, P. Gergaud, J.L. Lebrun, K. Ostolaza, V. Ji, X-ray study on single crystal superalloy SRR99: Mismatch γ/γ' ; mosaicity and internal stress, *Acta Mater.* 45 (2) (1997) 791–800.
- S. Shinde, P. Shinde, S. Pawar, A. Moholkar, C. Bhosale, K. Rajpure, Physical properties of transparent and conducting sprayed fluorine doped zinc oxide thin films, *Solid State Sci.* 10 (9) (2008) 1209–1214.
- E. Puyoo, G. Rey, E. Appert, V. Consonni, D. Bellet, Efficient dye-sensitized solar cells made from ZnO nanostructure composites, *J. Phys. Chem. C* 116 (34) (2012) 18117–18123.
- H. Koyama, Y. Saito, The crystal structure of zinc oxyacetate, Zn₄O(CH₃COO)₆, *Bull. Chem. Soc. Jpn.* 27 (2) (1954) 112–114.
- D. Lin, W. Pan, H. Wu, Morphological control of centimeter long aluminum-doped zinc oxide nanofibers prepared by electrospinning, *J. Am. Ceram. Soc.* 90 (1) (2007) 71–76.
- P.M.R. Kumar, C.S. Kartha, K.P. Vijayakumar, T. Abe, Y. Kashiwaba, F. Singh, D.K. Avasthi, On the properties of indium doped ZnO thin films, *Semicond. Sci. Technol.* 20 (2) (2005) 120.
- K. Moh Lin, Y.-Y. Chen, K.-Y. Chou, Solution derived Al-doped zinc oxide films: doping effect, microstructure and electrical property, *J. Sol-Gel Sci. Technol.* 49 (2) (2009) 238–242.
- N.P. Dasgupta, S. Neubert, W. Lee, O. Trejo, J.-R. Lee, F.B. Prinz, Atomic layer deposition of Al-doped ZnO films: effect of grain orientation on conductivity, *Chem. Mater.* 22 (16) (2010) 4769–4775.
- F.K. Shan, B.I. Kim, G.X. Liu, Z.F. Liu, J.Y. Sohn, W.J. Lee, B.C. Shin, Y.S. Yu, Blueshift of near band edge emission in Mg doped ZnO thin films and aging, *J. Appl. Phys.* 95 (9) (2004) 4772.
- X. Jiang, C.L. Jia, R.J. Hong, Microstructure dependence of ZnO:Al films on the deposition conditions and the surface morphology of silicon substrate, *J. Cryst. Growth* 289 (2) (2006) 464–471.
- W. Böttler, V. Smirnov, J. Hüpkes, F. Finger, Texture-etched ZnO as a versatile base for optical back reflectors with well-designed surface morphologies for application in thin film solar cells, *Phys. Status Solidi A* 209 (6) (2012) 1144–1149.
- J.L. Owen, W. Zhang, D. Köhl, J. Hüpkes, Study on the in-line sputtering growth and structural properties of polycrystalline ZnO:Al on ZnO and glass, *J. Cryst. Growth* 344 (1) (2012) 12–18.
- S. Maniv, W.D. Westwood, E. Colombini, Pressure and angle of incidence effects in reactive planar magnetron sputtered ZnO layers, *J. Vac. Sci. Technol.* 20 (2) (1982) 162–170.
- P. Sagar, M. Kumar, R. Mehra, Electrical and optical properties of sol–gel derived ZnO:Al thin films, *Mater. Sci. Pol.* 23 (3) (2005) 685.
- S.S. Shinde, P.S. Shinde, C.H. Bhosale, K.Y. Rajpure, Optoelectronic properties of sprayed transparent and conducting indium doped zinc oxide thin films, *J. Phys. D: Appl. Phys.* 41 (10) (2008) 105109.
- T. Wei, Y. Zhang, Y. Yang, R. Tan, P. Cui, W. Song, Effects of ZnAl₂O₄ segregation in high temperature sintered Al-doped ZnO sputtering target on optical and electrical properties of deposited thin films, *Surf. Coat. Technol.* 221 (2013) 201–206.
- M. Lucio-López, A. Maldonado, R. Castaneda-Pérez, G. Torres-Delgado, M. de la L. Olvera, Thickness dependence of ZnO:In thin films doped with different indium compounds and deposited by chemical spray, *Sol. Energy Mater. Sol. Cells* 90 (15) (2006) 2362–2376.
- M.H. Huang, S. Mao, H. Feick, H. Yan, Y. Wu, H. Kind, E. Weber, R. Russo, P. Yang, Room-temperature ultraviolet nanowire nanolasers, *Science* 292 (5523) (2001) 1897–1899.
- N. Fujimura, T. Nishihara, S. Goto, J. Xu, T. Ito, Control of preferred orientation for ZnO_x films: control of self-texture, *J. Cryst. Growth* 130 (12) (1993) 269–279.
- S.-S. Lin, J.-L. Huang, Effect of thickness on the structural and optical properties of ZnO films by R.F. magnetron sputtering, *Surf. Coat. Technol.* 185 (23) (2004) 222–227.
- J. Perrière, E. Millon, W. Seiler, C. Boulmer-Leborgne, V. Craciun, O. Albert, J.C. Loulergue, J. Etchepare, Comparison between ZnO films grown by femtosecond and nanosecond laser ablation, *J. Appl. Phys.* 91 (2) (2002) 690–696.
- B.-Z. Dong, G.-J. Fang, J.-F. Wang, W.-J. Guan, X.-Z. Zhao, Effect of thickness on structural, electrical, and optical properties of ZnO:Al films deposited by pulsed laser deposition, *J. Appl. Phys.* 101 (3) (2007) 033713.
- A. Van der Drift, Evolutionary selection, a principle governing growth orientation in vapour-deposited layers, *Philips Res. Rep.* 22 (3) (1967) 267–288.
- R.C. Cammarata, T.M. Trimble, D.J. Srolovitz, Surface stress model for intrinsic stresses in thin films, *J. Mater. Res.* 15 (2000) 2468–2474.
- E. Chason, B.W. Sheldon, L.B. Freund, J.A. Floro, S.J. Hearne, Origin of compressive residual stress in polycrystalline thin films, *Phys. Rev. Lett.* 88 (2002) 156103.
- B.W. Sheldon, K.H.A. Lau, A. Rajamani, Intrinsic stress, island coalescence, and surface roughness during the growth of polycrystalline films, *J. Appl. Phys.* 90 (10) (2001) 5097–5103.
- Y. Igasaki, H. Saito, Substrate temperature dependence of electrical properties of ZnO:Al epitaxial films on sapphire (1210), *J. Appl. Phys.* 69 (4) (1991) 2190–2195.
- Y. Igasaki, H. Saito, The effects of deposition rate on the structural and electrical properties of ZnO:Al films deposited on (120) oriented sapphire substrates, *J. Appl. Phys.* 70 (7) (1991) 3613–3619.
- T.P. Rao, M. Santhoshkumar, Effect of thickness on structural, optical and electrical properties of nanostructured ZnO thin films by spray pyrolysis, *Appl. Surf. Sci.* 255 (8) (2009) 4579–4584.
- A.P. Roth, J.B. Webb, D.F. Williams, Band-gap narrowing in heavily defect-doped ZnO, *Phys. Rev. B* 25 (1982) 7836–7839.
- B.E. Sernelius, K.-F. Berggren, Z.-C. Jin, I. Hamberg, C.G. Granqvist, Band-gap tailoring of ZnO by means of heavy Al doping, *Phys. Rev. B* 37 (1988) 10244–10248.
- V. Aquilanti, K. Mundim, S. Cavalli, D.D. Fazio, A. Aguilar, J. Lucas, Exact activation energies and phenomenological description of quantum tunneling for model potential energy surfaces. The F + H₂ reaction at low temperature, *Chem. Phys.* 398 (2012) 186–191.
- A. Janotti, C.G.V. de Walle, Fundamentals of zinc oxide as a semiconductor, *Rep. Prog. Phys.* 72 (12) (2009) 126501.
- F. Garcés, L. Acquaroli, R. Urteaga, A. Dussan, R. Koropecski, R. Arce, Structural properties of porous silicon/SnO₂:F heterostructures, *Thin Solid Films* 520 (13) (2012) 4254–4258.
- L.A. Balagurov, S.C. Bayliss, A.F. Orlov, E.A. Petrova, B. Unal, D.G. Yarkin, Electrical properties of metal/porous silicon/p-Si structures with thin porous silicon layer, *J. Appl. Phys.* 90 (8) (2001) 4184–4190.